Journal of Zhejiang University-SCIENCE A (Applied Physics & Engineering) 2023 24(7):637-652
www.jzus.zju.edu.cn; www.springer.com/journal/11582
E-mail: jzus_a@zju.edu.cn

Research Article

https://doi.org/10.1631/jzus.A2200385

Analytical solution of ground-borne vibration due to a spatially periodic harmonic moving load in a tunnel embedded in layered soil

Lihui XU[1,2], Meng MA[1,2]✉

[1]*Key Laboratory of Urban Underground Engineering of Ministry of Education, Beijing Jiaotong University, Beijing 100044, China*
[2]*School of Civil Engineering, Beijing Jiaotong University, Beijing 100044, China*

Abstract: In this study, we propose a novel coupled periodic tunnel–soil analytical model for predicting ground-borne vibrations caused by vibration sources in tunnels. The problem of a multilayered soil overlying a semi-infinite half-space was solved using the transfer matrix method. To account for the interactions between the soil layer and tunnel structure, the transformation characteristics between cylindrical waves and plane waves were considered and used to convert the corresponding wave potentials into forms in terms of the Cartesian or cylindrical coordinate system. The induced ground-borne vibration was obtained analytically by applying a spatially periodic harmonic moving load to the tunnel invert. The accuracy and efficiency of the proposed model were verified by comparing the results under a moving constant and harmonic load with those from previous studies. Subsequently, the response characteristics under a spatially periodic harmonic moving load were identified, and the effects of a wide range of factors on the responses were systematically investigated. The numerical results showed that moving and Doppler effects can be caused by a spatially periodic harmonic moving load. The critical frequency and frequency bandwidth of the response are affected by the load type, frequency, velocity, and wavenumber in one periodicity length. Increasing the tunnel depth is an efficient way to reduce ground-borne vibrations. The effect of vibration amplification on the free surface should be considered to avoid excessive vibration levels that disturb residents.

Key words: Coupled tunnel–soil model; Spatially periodic load; Transfer matrix method; Wave transformation; Parametric analysis

1 Introduction

With the rapid construction of subway tunnels in metropolitan cities, the environmental problem of ground-borne vibrations induced by underground trains has attracted widespread attention in recent decades (Lopes et al., 2016; Zhang et al., 2018; Liu et al., 2022; Ma et al., 2022; Xu et al., 2022). Investigations on this topic are helpful for evaluating and easing the impact of train-induced vibration on adjacent residents, historical buildings, and sensitive instruments (Hussein and Hunt, 2009; Ma et al., 2016; Jin et al., 2022; Zou et al., 2022). A train-induced discretely distributed force through fasteners satisfies the periodicity conditions. Thus, it can be further decomposed into a series of spatially periodic harmonic moving loads (Doyle, 1997) and is a periodic problem. To solve this problem, we propose a tunnel–soil coupled analytical model that is periodic in the longitudinal direction. The model and the characteristics of ground-borne vibrations under a spatially periodic harmonic moving load are presented in this study.

Numerical methods are most commonly used to investigate ground-borne vibrations from underground sources. Two main issues need to be addressed in numerical simulations (Xu et al., 2022): (1) boundary truncation error, and (2) calculation efficiency. In previous studies, different inspiring models have been proposed to overcome these issues. For instance, the boundary truncation error was avoided by the infinite element (IFE) technique (Lin et al., 2016; Yang et al., 2017, 2021; Yang and Li, 2022), and the calculation efficiency was improved by using 2.5D approaches (Sheng et al., 2005; François et al., 2010; Gao et al., 2011; Zhou et al., 2019; Ma et al., 2021). Periodic numerical models were

✉ Meng MA, mameng@bjtu.edu.cn

Received Aug. 11, 2022; Revision accepted Dec. 16, 2022;
Crosschecked May 9, 2023; Online first June 16, 2023

also proposed (Clouteau et al., 2005; Degrande et al., 2006; Ma et al., 2017; Xu et al., 2022). More exhaustive summaries of models for predicting vibrations from underground sources have been reported in the literature (Kouroussis et al., 2014; Lombaert et al., 2015; Ma et al., 2020). However, numerical calculation still requires huge computer memory and computational time.

An analytical model is the most efficient way to investigate ground vibrations from underground sources accurately and rapidly as there are no boundary truncations or approximations. Various analytical models have been proposed in previous studies. A 2D analytical model (Metrikine and Vrouwenvelder, 2000) and the pipe-in-pipe (PiP) semi-analytical model (Forrest and Hunt, 2006a, 2006b; Hussein et al., 2014) are the most well-known. Recently, Yuan et al. (2017) proposed a closed-form semi-analytical model to obtain a benchmark solution for ground vibration from an underground point source moving in a tunnel embedded in a homogeneous half-space. In this model, the soil–tunnel interaction was represented by transformations between ascending and descending plane waves and outgoing and regular cylindrical waves, as proposed by Boström et al. (1991). This approach was then extended to cover the case in which a tunnel was embedded in a multilayered half-space (He et al., 2018). A coupled train–track model was also considered (Yuan et al., 2021), and the interactions between twin tunnels were simulated (He et al., 2019). Notably, all these analytical models were homogeneous in the longitudinal direction. No analytical periodic models for coupled tunnel–soil systems have yet been proposed.

In the dynamic problem of a coupled tunnel–soil system, two main issues remain and need to be addressed when the coupled system is periodic in the longitudinal direction. These issues include further improvement of the calculation efficiency of numerical periodic models, and accurate solution of the periodicity problem in analytical models. This work focused on the 2nd issue. To this end, in this study we extended the coupled tunnel–soil analytical model proposed by Yuan et al. (2017) and He et al. (2018) by investigating, with the aid of generalised modal function series, the case in which a tunnel–soil system is periodic in the longitudinal direction. This study is the first attempt to solve the periodicity problem of a coupled tunnel–soil system analytically.

We propose a coupled periodic tunnel–soil analytical model to characterise dynamic ground-borne vibration under a spatially periodic harmonic moving load. Based on the generalised modal functions and Fourier transform, the general solutions of the displacements and tractions for each soil layer and tunnel structure were derived in the frequency-generalised wavenumber domain. The horizontally layered soils were then modeled using the transfer matrix method to obtain the relationship between the coefficients for each layer. The interaction between the soil and tunnel was realised by considering the properties of the transformation between plane and cylindrical waves. The dynamic response for each part of this model was calculated by applying a spatially periodic harmonic moving load to the inverted arch of the inner surface of the tunnel. Subsequently, the accuracy and efficiency of the model were demonstrated by comparing the results under a moving constant and harmonic load with those from the literature (Yuan et al., 2017; He et al., 2018). Finally, the results of the ground-borne vibrations under spatially periodic harmonic moving loads are presented, along with those from a systematic investigation of the effects of a wide range of factors on the vibration responses. Some conclusions are drawn based on the analyses and discussion.

2 Formulation of the coupled periodic tunnel–soil analytical model

2.1 Model description

Fig. 1 illustrates a tunnel embedded in a multilayered half-space in the global coordinate system. The model is periodic and comprises N+1 parts, including N−2 standard interior soil layers where both ascending and descending waves exist, one interior layer n with a cavity where ascending, descending, and outgoing (irregular) waves exist, one semi-infinite region N where only descending waves exist, and one hollow cylinder for the tunnel where outgoing and regular waves exist. In each part, the interfaces are bonded with their adjoining parts, implying that tractions and deflections can be directly transferred to the adjoining parts. An external force p that is periodic in space with periodicity length L and harmonic in time with circular frequency ω_1 is applied at the bottom of the inner surface of the hollow cylinder and moves toward the positive z-axis

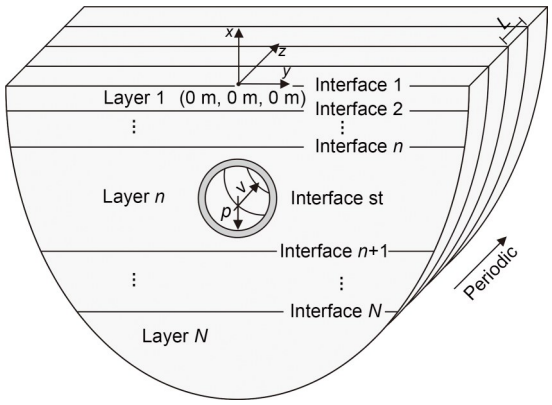

Fig. 1 Tunnel embedded in a multilayered half-space subjected to a spatially periodic harmonic moving load *p* in a global coordinate system. The interface st represents the connection between the hollow cylinder and the layer with a cavity

at a constant speed of v. The material of each part is assumed to be isotropic, homogeneous, and viscoelastic. Therefore, integral transformation and superposition techniques can be applied in this case. Because the applied force is periodic in the z-direction, the entire system is periodic in the z-direction.

The geometry, local coordinate system, and state variables along the interface for each part are shown in Fig. 2. These parts can be sub-divided into four components: a standard layer, a semi-infinite region, a layer with a cavity, and a hollow cylinder. In the Cartesian coordinate, the state variable $\hat{\tilde{\boldsymbol{S}}}$ is defined as the collection of the displacement vector $\hat{\tilde{\boldsymbol{u}}}=\left[\hat{\tilde{u}}_x,\ \hat{\tilde{u}}_y,\ \hat{\tilde{u}}_z\right]^{\mathrm{T}}$ and traction vector $\hat{\tilde{\boldsymbol{\sigma}}}=\left[\hat{\tilde{\sigma}}_{xx},\ \hat{\tilde{\sigma}}_{xy},\ \hat{\tilde{\sigma}}_{xz}\right]^{\mathrm{T}}$ expressed as $\hat{\tilde{\boldsymbol{S}}}=\left[\hat{\tilde{\boldsymbol{u}}}^{\mathrm{T}}\ \hat{\tilde{\boldsymbol{\sigma}}}^{\mathrm{T}}\right]^{\mathrm{T}}$. In the cylindrical coordinate, the state variable $\bar{\tilde{\boldsymbol{S}}}^m$ is expressed as $\bar{\tilde{\boldsymbol{S}}}^m=\left[\bar{\tilde{\boldsymbol{u}}}^{m\,\mathrm{T}}\ \bar{\tilde{\boldsymbol{\sigma}}}^{m\,\mathrm{T}}\right]^{\mathrm{T}}$ where $\bar{\tilde{\boldsymbol{u}}}^m=\left[\bar{\tilde{u}}_r^m,\ \bar{\tilde{u}}_\varphi^m,\ \bar{\tilde{u}}_z^m\right]^{\mathrm{T}}$ and $\bar{\tilde{\boldsymbol{\sigma}}}^m=\left[\bar{\tilde{\sigma}}_{rr}^m,\ \bar{\tilde{\sigma}}_{r\varphi}^m,\ \bar{\tilde{\sigma}}_{rz}^m\right]^{\mathrm{T}}$.

2.2 Formulation of the analytical periodic model

The motion of the isotropic, homogeneous, and viscoelastic continuum is governed by the free elastodynamics equation, expressed in vector form as (Sheng et al., 2002):

$$\mu\nabla^2\boldsymbol{u}+(\lambda+\mu)\nabla(\nabla\cdot\boldsymbol{u})=\rho\ddot{\boldsymbol{u}}, \tag{1}$$

where $\boldsymbol{u}$ is the displacement vector expressed in Cartesian coordinates $\boldsymbol{u}=[u_x, u_y, u_z]^{\mathrm{T}}$, or in cylindrical coordinates $\boldsymbol{u}=[u_r, u_\varphi, u_z]^{\mathrm{T}}$. ρ is the density of the material. The symbol "¨" denotes the 2nd-order derivative with respect to time t. λ and μ are the Lamé constants. Considering nondimensional material damping ζ, the Lamé constants can be rewritten as $\lambda=\lambda(1+\mathrm{i}\zeta)$ and $\mu=\mu(1+\mathrm{i}\zeta)$.

To solve this equation in the frequency-wavenumber-generalised modal space, the Fourier transforms with respect to time t and coordinate y, and the generalised model superposition technique (Hussein and Hunt, 2009; Ma and Liu, 2018) regarding coordinate z are used as follows:

$$\begin{aligned}\tilde{f}(\omega)&=\int_{-\infty}^{+\infty}f(t)\,\mathrm{e}^{-\mathrm{i}\omega t}\mathrm{d}t,\\ f(t)&=\frac{1}{2\pi}\int_{-\infty}^{+\infty}\tilde{f}(\omega)\,\mathrm{e}^{\mathrm{i}\omega t}\mathrm{d}\omega,\end{aligned} \tag{2}$$

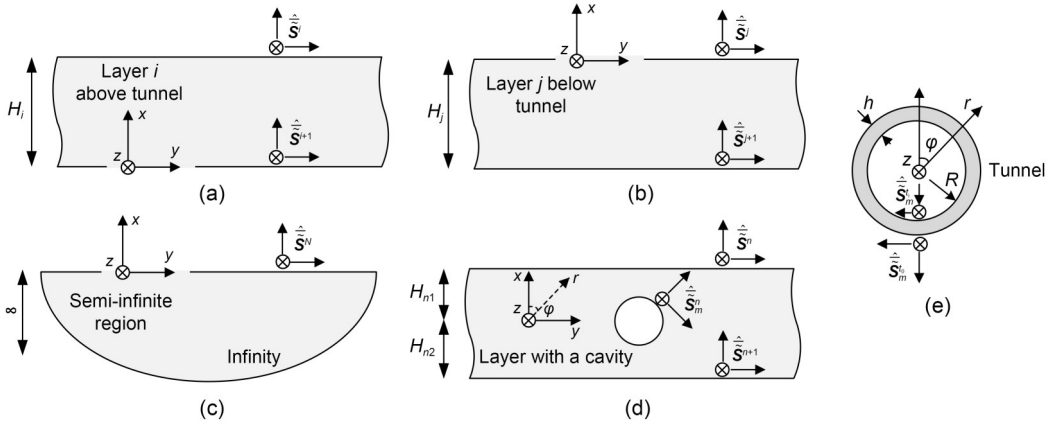

Fig. 2 Geometry, local coordinate system, and state variable at the corresponding interface of the soil layer: (a) layer above the tunnel (*i*<*n*); (b) layer below the tunnel (*j*>*n*); (c) semi-infinite region, layer *N*; (d) layer *n* with a cavity; (e) hollow cylinder for tunnel lining

$$\begin{aligned}\hat{f}\left(k_y\right)&=\int_{-\infty}^{+\infty}f(y)\,\mathrm{e}^{-\mathrm{i}k_y y}\mathrm{d}y,\\ f(y)&=\frac{1}{2\pi}\int_{-\infty}^{+\infty}\hat{f}\left(k_y\right)\mathrm{e}^{\mathrm{i}k_y y}\mathrm{d}k_y,\end{aligned}\tag{3}$$

$$\tilde{R}(z,\,\omega,\,\omega_1)=\sum_{n_1=-\infty}^{n_1=+\infty}\bar{\tilde{R}}_{n_1}(\omega)\,\Phi_{n_1}(z,\,\omega_1,\,\omega),\tag{4}$$

where k_y is the wavenumber, ω_1 is the harmonic load frequency, $\tilde{R}$ is an arbitrary periodic function regarding z, $\bar{\tilde{R}}$ is the transformation coefficient of $\tilde{R}$, and $\Phi_{n_1}(z,\,\omega_1,\omega)$ is the generalised modal function, which takes the following form:

$$\Phi_{n_1}(z,\,\omega_1,\,\omega)=\mathrm{e}^{\mathrm{i}\lambda_{n_1}z},\quad \lambda_{n_1}=\frac{2\pi n_1}{L}+\frac{\omega_1-\omega}{v}.\tag{5}$$

With the aid of Eqs. (2)–(4), the expressions for displacements and stresses in both Cartesian and cylindrical coordinate systems derived in terms of the wave potential functions by Pilant (1979) can be directly applied to obtain general solutions. Displacements and stresses in the frequency-wavenumber domain are expressed according to the plane wave potentials $\hat{\bar{\boldsymbol{\phi}}}$ and $\hat{\bar{\boldsymbol{\varphi}}}$, and the cylindrical wave potentials $\bar{\tilde{\boldsymbol{\chi}}}^m$ and $\bar{\tilde{\boldsymbol{\eta}}}^m$, respectively.

For the standard interior soil layer (Figs. 2a and 2b), the state variable $\hat{\bar{\tilde{\boldsymbol{S}}}}^l$ (l=i or j) written in matrix form is:

$$\hat{\bar{\tilde{\boldsymbol{S}}}}^l(x^l)=\left[\hat{\bar{\tilde{\boldsymbol{u}}}}^{\mathrm{T}}\ \hat{\bar{\tilde{\boldsymbol{\sigma}}}}^{\mathrm{T}}\right]^{\mathrm{T}}=\begin{bmatrix}\hat{\bar{\boldsymbol{\phi}}}_{\mathrm{a}}(x^l) & \hat{\bar{\boldsymbol{\phi}}}_{\mathrm{d}}(x^l)\\ \hat{\bar{\boldsymbol{\varphi}}}_{\mathrm{a}}(x^l) & \hat{\bar{\boldsymbol{\varphi}}}_{\mathrm{d}}(x^l)\end{bmatrix}\begin{bmatrix}\boldsymbol{A}_{\mathrm{a}}^l\\ \boldsymbol{A}_{\mathrm{d}}^l\end{bmatrix}=\boldsymbol{M}(x^l)\,\boldsymbol{A}^l,\tag{6}$$

where the superscript l denotes the lth layer (l=i or j), and x^l is the x-coordinate in the local coordinate system, as shown in Fig. 2. $\hat{\bar{\boldsymbol{\phi}}}_{\mathrm{a}}(x^l)=\left[\hat{\bar{\boldsymbol{\phi}}}_{\mathrm{a1}}(x^l)\ \ \hat{\bar{\boldsymbol{\phi}}}_{\mathrm{a2}}(x^l)\ \ \hat{\bar{\boldsymbol{\phi}}}_{\mathrm{a3}}(x^l)\right]$. The subscripts a and d mean ascending and descending waves, respectively. The other matrices have similar matrix forms. $\boldsymbol{A}_{\mathrm{a}}^{\,l}$ and $\boldsymbol{A}_{\mathrm{d}}^{\,l}$ are the respective ascending and descending wave coefficient vectors. $\boldsymbol{M}(x^l)=\begin{bmatrix}\hat{\bar{\boldsymbol{\phi}}}_{\mathrm{a}}(x^l) & \hat{\bar{\boldsymbol{\phi}}}_{\mathrm{d}}(x^l)\\ \hat{\bar{\boldsymbol{\varphi}}}_{\mathrm{a}}(x^l) & \hat{\bar{\boldsymbol{\varphi}}}_{\mathrm{d}}(x^l)\end{bmatrix}$ is a wave potential matrix.

Considering the boundary, compatibility, and equilibrium conditions, the relationships of the unknown coefficients of each layer can be derived by applying the transfer matrix method. The compatibility and equilibrium conditions are

$$\hat{\bar{\tilde{\boldsymbol{S}}}}^{i-1}(x^{i-1}=0)=\hat{\bar{\tilde{\boldsymbol{S}}}}^{i}(x^{i}=H_i),\quad i<n,\tag{7}$$

$$\hat{\bar{\tilde{\boldsymbol{S}}}}^{j}\left(x^{j}=-H_j\right)=\hat{\bar{\tilde{\boldsymbol{S}}}}^{j+1}(x^{j+1}=0),\quad j>n.\tag{8}$$

The relationship between the unknown coefficients $\boldsymbol{A}^1$ of the layer 1 and $\boldsymbol{A}^{n-1}$ of the layer $n-1$ can be derived as follows:

$$\boldsymbol{A}^1=\boldsymbol{T}_{(1,n-1)}\boldsymbol{A}^{n-1},\tag{9}$$

where $\boldsymbol{T}_{(1,n-1)}$ is the transfer matrix.

Similarly, the relationship between the coefficients $\boldsymbol{A}^N$ of the layer N and $\boldsymbol{A}^{n+1}$ of the layer n+1 can be derived as follows:

$$\boldsymbol{A}^N=\boldsymbol{T}_{(N,n+1)}\boldsymbol{A}^{n+1},\tag{10}$$

where $\boldsymbol{T}_{(N,n+1)}$ is the transfer matrix.

To couple the standard layer and the layer with a cavity, the outgoing cylindrical wave $\bar{\tilde{\boldsymbol{\chi}}}_{\mathrm{o}j}^m$ should be converted into ascending or descending plane waves, obeying the following relationships proposed by Boström et al. (1991):

$$\begin{aligned}\bar{\tilde{\boldsymbol{\chi}}}_{\mathrm{o}j}^m&=\frac{1}{\pi}\int_{-\infty}^{+\infty}\frac{\hat{\bar{\tilde{\boldsymbol{\phi}}}}_{\mathrm{a}j}\mathrm{e}^{\mathrm{i}k_y y}}{k_{xj}}T_{mj}^{-}\mathrm{d}k_y,\\ \bar{\tilde{\boldsymbol{\chi}}}_{\mathrm{o}j}^m&=\frac{1}{\pi}\int_{-\infty}^{+\infty}\frac{\hat{\bar{\tilde{\boldsymbol{\phi}}}}_{\mathrm{d}j}\mathrm{e}^{\mathrm{i}k_y y}}{k_{xj}}T_{mj}^{+}\mathrm{d}k_y,\end{aligned}\tag{11}$$

where k_{xj} is the wavenumber in the x-direction, $\hat{\bar{\tilde{\boldsymbol{\phi}}}}_{\mathrm{a}j}$ and $\hat{\bar{\tilde{\boldsymbol{\phi}}}}_{\mathrm{d}j}$ are the ascending and descending plane wave potentials for displacements, respectively, and T_{mj}^{+} and T_{mj}^{-} are explained in Eq. (S29) of the electronic supplementary materials (ESM). Then, the state variables of the upper and lower interfaces in layer n with a cavity can be obtained. Considering the compatibility and equilibrium conditions along the upper and lower interfaces of the layer with a cavity with adjoining layers, the relationships between $\boldsymbol{A}^n$ and $\boldsymbol{A}_{\mathrm{o}}$, and between $\boldsymbol{A}^1$ and $\boldsymbol{A}_{\mathrm{o}}$ can be derived, respectively, as:

$$\boldsymbol{A}^n=\begin{bmatrix}\boldsymbol{A}^n_{\mathrm{a}}\\ \boldsymbol{A}^n_{\mathrm{d}}\end{bmatrix}=\boldsymbol{T}_{(\boldsymbol{A}^n,\boldsymbol{A}_{\mathrm{o}})}\boldsymbol{A}_{\mathrm{o}}=\begin{bmatrix}\boldsymbol{T}^{\mathrm{a}}\\ \boldsymbol{T}^{\mathrm{d}}\end{bmatrix}\boldsymbol{A}_{\mathrm{o}}, \tag{12}$$

$$\boldsymbol{A}^1=\boldsymbol{T}_{(\boldsymbol{A}^1,\boldsymbol{A}_{\mathrm{o}})}\boldsymbol{A}_{\mathrm{o}}, \tag{13}$$

where $\boldsymbol{A}_{\mathrm{o}}$ is the unknown vector, the matrices $\boldsymbol{T}_{(\boldsymbol{A}^n,\boldsymbol{A}_{\mathrm{o}})}$ and $\boldsymbol{T}_{(\boldsymbol{A}^1,\boldsymbol{A}_{\mathrm{o}})}$ both have the dimensions 6×3(M+1), $\boldsymbol{T}^{\mathrm{a}}$ and $\boldsymbol{T}^{\mathrm{d}}$ are transfer coefficient matrices with dimensions 3×3(M+1), and M is the number of trigonometric terms.

To couple the layer with a cavity and hollow cylinder, the ascending and descending plane wave potentials should be expanded in terms of regular cylindrical wave potentials, expressed as (Boström et al., 1991):

$$\hat{\bar{\boldsymbol{\phi}}}_{\mathrm{aj}}\mathrm{e}^{\mathrm{i}k_y y}=\sum_{m=0}^{M}\varepsilon_m\bar{\bar{\boldsymbol{\chi}}}^m_{\mathrm{rj}}T^+_{mj},\quad \hat{\bar{\boldsymbol{\phi}}}_{\mathrm{dj}}\mathrm{e}^{\mathrm{i}k_y y}=\sum_{m=0}^{M}\varepsilon_m\bar{\bar{\boldsymbol{\chi}}}^m_{\mathrm{rj}}T^-_{mj}, \tag{14}$$

where ε_m=1 when m=0 and ε_m=2 when m≠0.

The displacement and traction vector along the outer interface (r=R+h) of the cavity can then be obtained. According to the compatibility and equilibrium conditions along the interface, the unknown coefficients $\boldsymbol{B}^m$ for the tunnel structure and $\boldsymbol{A}_{\mathrm{o}}$ for the layer with a cavity are related by:

$$\boldsymbol{B}^m=\begin{bmatrix}\bar{\bar{\boldsymbol{\chi}}}^m_{\mathrm{o}}(r=R+h) & \bar{\bar{\boldsymbol{\chi}}}^m_{\mathrm{r}}(r=R+h)\\ \bar{\bar{\boldsymbol{\eta}}}^m_{\mathrm{o}}(r=R+h) & \bar{\bar{\boldsymbol{\eta}}}^m_{\mathrm{r}}(r=R+h)\end{bmatrix}^{-1}\cdot\begin{bmatrix}\boldsymbol{C}^n_m(r=R+h)\\ \boldsymbol{D}^n_m(r=R+h)\end{bmatrix}\boldsymbol{A}_{\mathrm{o}}, \tag{15}$$

where subscripts o and r are the outgoing and regular cylindrical waves, respectively; $\boldsymbol{C}^n_m$ and $\boldsymbol{D}^n_m$ are coefficient matrices.

2.3 Moving load applied at the inner interface of the tunnel structure

The applied external load is periodic in space with a periodicity length L, harmonic in time with a circular frequency ω_{l}, and moves at a constant speed of v in the z-direction. The force applied at the inverted arch of the tunnel structure can be mathematically expressed as (Xu and Ma, 2022):

$$p(r,\varphi,z,t)=\frac{1}{R}\delta(r-R)\delta(\varphi-\pi)\delta(z-vt)\mathrm{e}^{\mathrm{i}\xi_{n_{\mathrm{l}}}z}\mathrm{e}^{\mathrm{i}\omega_{\mathrm{l}}t},\quad \xi_{n_{\mathrm{l}}}=\frac{2\pi n_{\mathrm{l}}}{L}, \tag{16}$$

where δ is the Dirac delta function.

The origin of the moving load is located at (R, π, 0 m). Performing a Fourier transform and considering the orthogonality of the generalised modal function, the external load vector at the tunnel invert $\bar{\bar{\boldsymbol{t}}}_m$ can be expressed as follows:

$$\bar{\bar{\boldsymbol{t}}}_m(r=R)=\begin{bmatrix}\bar{\tilde{p}}_m(r=R) & 0 & 0\end{bmatrix}^{\mathrm{T}},\quad \bar{\tilde{p}}_m(r=R)=\frac{\varepsilon_m}{2\pi vR}(-1)^m\delta(r-R)\cos(m\varphi). \tag{17}$$

According to the stress boundary condition of the inner interface of the tunnel structure, the following formulation can be obtained:

$$\begin{bmatrix}\bar{\bar{\boldsymbol{\eta}}}^m_{\mathrm{o}}(r=R) & \bar{\bar{\boldsymbol{\eta}}}^m_{\mathrm{r}}(r=R)\end{bmatrix}\boldsymbol{B}^m=\bar{\bar{\boldsymbol{t}}}_m(r=R). \tag{18}$$

Substituting Eq. (15) into Eq. (18) yields the following equation:

$$\begin{bmatrix}\bar{\bar{\boldsymbol{\eta}}}^m_{\mathrm{o}}(r=R) & \bar{\bar{\boldsymbol{\eta}}}^m_{\mathrm{r}}(r=R)\end{bmatrix}\cdot\begin{bmatrix}\bar{\bar{\boldsymbol{\chi}}}^m_{\mathrm{o}}(r=R+h) & \bar{\bar{\boldsymbol{\chi}}}^m_{\mathrm{r}}(r=R+h)\\ \bar{\bar{\boldsymbol{\eta}}}^m_{\mathrm{o}}(r=R+h) & \bar{\bar{\boldsymbol{\eta}}}^m_{\mathrm{r}}(r=R+h)\end{bmatrix}^{-1}\cdot\begin{bmatrix}\boldsymbol{C}^n_m(r=R+h)\\ \boldsymbol{D}^n_m(r=R+h)\end{bmatrix}\boldsymbol{A}_{\mathrm{o}}=\bar{\bar{\boldsymbol{t}}}_m(r=R). \tag{19}$$

This results in three equations for each m. After considering m=0, 1, 2, ⋯, M, there are 3(M+1) equations where there are 3(M+1) unknown $\boldsymbol{A}_{\mathrm{o}}$ as well. Thereafter, the unknown coefficients for the tunnel structure $\boldsymbol{B}^m$ and the first layer $\boldsymbol{A}^1$ can be derived based on Eqs. (15) and (13), respectively. The formulations derived above were programmed in MATLAB, where M=12 was considered to obtain the convergence result.

More detailed derivations can be obtained from Section S1 in the ESM.

3 Model validation

As observed in Eqs. (5) and (16), if the wavenumber in one periodicity length satisfies the condition n_{l}=0, the coupled periodic tunnel–soil analytical model is reduced to a model that is homogeneous in the longitudinal direction, as shown in many previous studies. To demonstrate the efficiency and accuracy of

our proposed model, the ground-borne vibrations from the model in which the tunnel is embedded in a homogeneous and multilayered half-space were compared with those from the literature (Yuan et al., 2017; He et al., 2018). Note that the tunnel is entirely embedded within a single soil layer. Validation cases, where the tunnel is embedded in a homogeneous and multilayered half-space, are illustrated in Fig. 3. The corresponding parameters involved in the validations are from the literature (Yuan et al., 2017; He et al., 2018). Further details are given in Section S2 in the ESM, where additional validation results are also presented.

First, the results from the model in which the tunnel is embedded in a homogeneous half-space (Fig. 3a) were compared with those obtained by Yuan et al. (2017), where the analytical method was adopted. In the longitudinal direction, the Fourier transform was applied because the soil was homogeneous in that direction according to Yuan et al. (2017).

Comparisons of the vibration responses at (0 m, 0 m, 0 m) and (0 m, 10 m, 0 m) of the ground surface under a constant load with frequency f_0=0 Hz moving at a speed of v=30 m/s with those from the analytical solution (Yuan et al., 2017) are illustrated in Figs. 4 and 5, respectively. As expected, the results were satisfactory in both the vertical and longitudinal directions. Impulsive effects were observed to be induced by the moving load. The vertical velocity reached zero, while the longitudinal velocity reached a maximum when the load moved to the position immediately beneath the observation section (t=0 s). The relative errors of the maximum absolute responses at (0 m, 0 m, 0 m) and (0 m, 10 m, 0 m) are listed with those from the analytical solutions (Yuan et al., 2017) in Table 1. The maximum relative error was about 2.39%, confirming the high accuracy of the method.

Second, validation was performed by comparing the results of the tunnel embedded in a multilayered half-space from the present method with those from the reference (He et al., 2018), as shown in Fig. 3b. In the analytical method by He et al. (2018), the coupled tunnel–soil system was regarded as homogeneous; thus, a Fourier transform was used.

A comparison of the vertical displacement frequency spectrum at (0 m, 10 m, 0 m) subjected to a moving load with v=50 m/s and frequencies of f_0=10 and

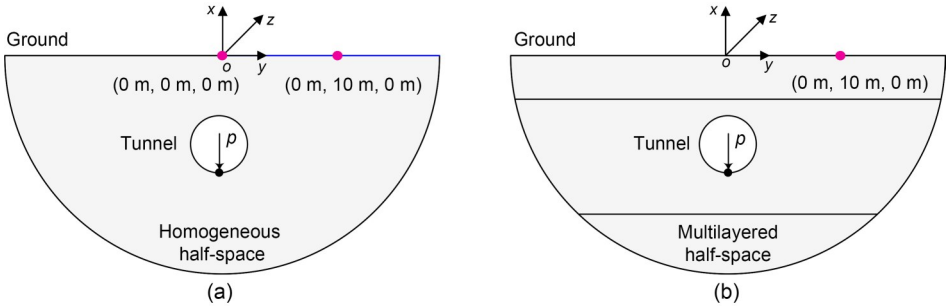

Fig. 3 Validation cases of a tunnel embedded in a homogeneous half-space (a) and a multilayered half-space (b)

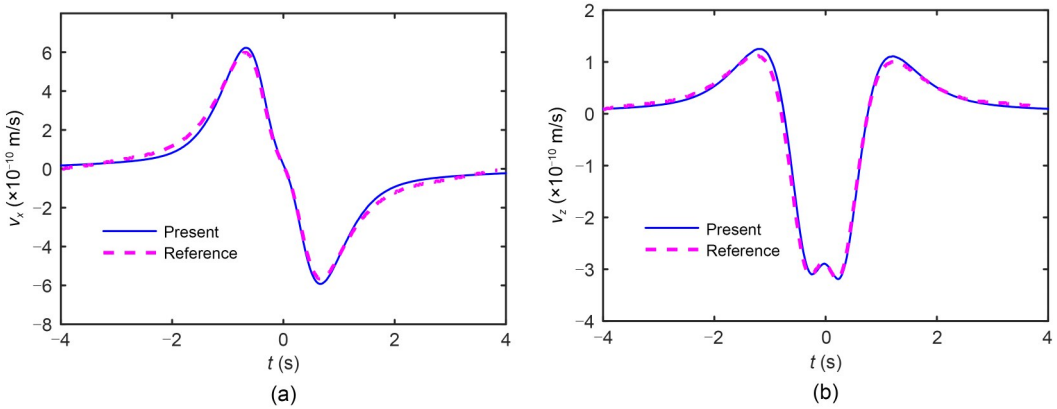

Fig. 4 Comparison of velocity history at (0 m, 0 m, 0 m) owing to moving constant load (v=30 m/s, f_0=0 Hz): (a) vertical direction, v_x; (b) longitudinal direction, v_z

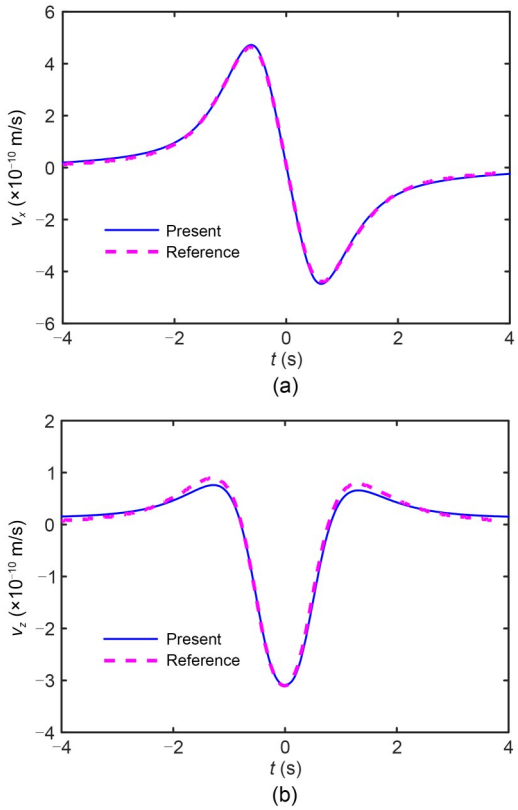

Fig. 5 Comparison of velocity history at (0 m, 10 m, 0 m) owing to moving constant load (v=30 m/s, f_0=0 Hz): (a) vertical direction, v_x; (b) longitudinal direction, v_z

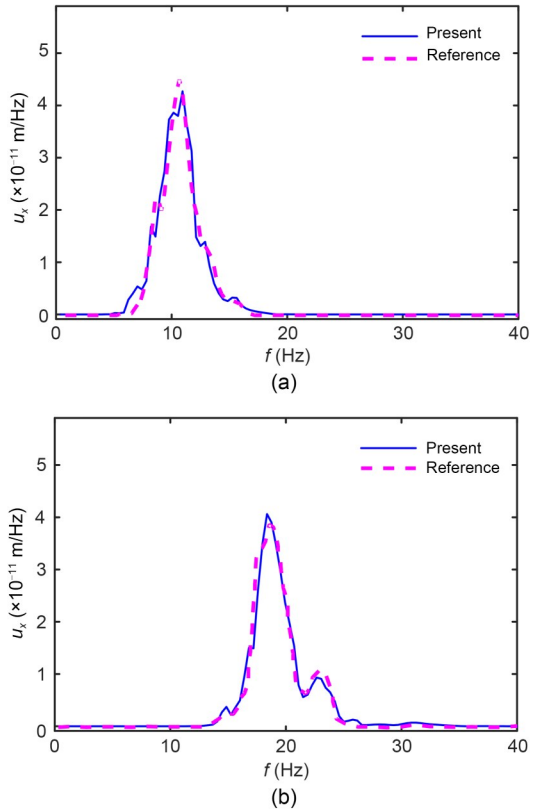

Fig. 6 Comparison of the vertical displacement frequency spectrum of the ground surface from a tunnel embedded in a multilayered half-space owing to a moving harmonic load with v=50 m/s: (a) f_0=10 Hz; (b) f_0=20 Hz

Table 1 Relative errors in the maximum absolute response obtained from the current method and the referenced solution

Location	Velocity direction	Relative error (%)
(0 m, 0 m, 0 m)	Vertical (v_x)	2.36
	Longitudinal (v_z)	0.31
(0 m, 10 m, 0 m)	Vertical (v_x)	2.01
	Longitudinal (v_z)	−0.32

20 Hz with the analytical solution (He et al., 2018) is plotted in Fig. 6. This indicates that the results from the present method are in good agreement with those from the reference. The frequency spreads mainly around the excitation frequency of the harmonic load. The Doppler effect induces a difference between the dominant frequencies of the response and excitation.

The proposed analytical model was run on a computer with an Intel(R) Core(TM) i7-7700K central processing unit (CPU) @ 4.20 GHz processor. Its computational time was about 39 s in the case of one calculation while that from the corresponding numerical model is several hours. The memory requirement was about 0.5 GB of random access memory (RAM). Therefore, this model requires low computer memory and computational time. These features have the potential to be applied in a quick environmental vibration assessment.

By comparing the results with those from previous studies, the accuracy and efficiency of the present analytical model, which is periodic in the longitudinal direction, were fully validated.

4 Numerical results and discussion

The ground vibration responses from the tunnel embedded in the multilayered half-space under a spatially periodic harmonic load were systematically investigated using the proposed coupled tunnel–soil periodic model. The dynamic parameters of the soil and tunnel were selected from the study of Xu and Ma (2020), in which a statistical survey of the geological parameters in Beijing was conducted. The soil parameters are listed in Table 2. Young's modulus of the tunnel structure was E=32 GPa, Poisson's ratio ν=0.2, material density

Table 2 Parameters of soil layers used in the investigation

Soil	c_s (m/s)	c_p (m/s)	ρ (kg/m^3)	ζ	H (m)
Layer 1	160	320	2000	0.1	5
Layer 2	260	520	2000	0.1	20
Semi-infinite region	320	640	2000	0.1	∞

$c_s=\sqrt{\mu/\rho}$; $c_p=\sqrt{(\lambda+2\mu)/\rho}$

ρ=2400 kg/m^3, and hysteretic material damping ζ=0.02. The axis of the tunnel was located in the 2nd soil layer at a depth of d=15 m from the ground surface. The tunnel structure had an inner radius of R=3 m and a thickness of h=0.3 m. Unless otherwise specified, these parameters were used in the following calculations. The number of trigonometric terms, M=12, was considered to provide a convergence result. When performing the inverse Fourier transform, a frequency range of $[-2f_{cr}, 2f_{cr}]$, where the response in the frequency range of f<0 Hz is conjugate with the counterpart at a frequency of f>0 Hz, was considered to yield a real response in the time domain. The critical frequency f_{cr} was defined as the frequency around which the response frequency mainly spreads. A moving load was imposed at the inverted arch of the tunnel. Note that some additional results and discussion are presented in Section S3 in the ESM.

4.1 General results

The general response of the ground surface under a spatially periodic harmonic moving load (n_1=1, f_0= 5 Hz, v=25 m/s) is presented in this section. The load velocity approximately corresponds to the maximum design velocity of the metro in Beijing, China.

The displacement responses at points A (0 m, 0 m, 0 m) and B (0 m, 10 m, 0 m) on the ground surface in both the time and frequency domains are shown in Fig. 7. In the time domain, the ground point experiences an about 2-s dynamic vibration because the propagating waves radiate outwards from the tunnel. Both the vertical and longitudinal displacements are not perfectly symmetric with respect to t=0 s because of damping and Doppler effects. The vertical displacement exhibited a different time history from that of the longitudinal displacement. At the time instant t=0 s, when the load moved to the point immediately beneath point A, the vertical vibration amplitude reached a maximum, while the longitudinal vibration reached zero. The vertical vibration was stronger than the longitudinal vibration because the applied load at the tunnel invert was vertical. Overall, the displacement responses exhibited

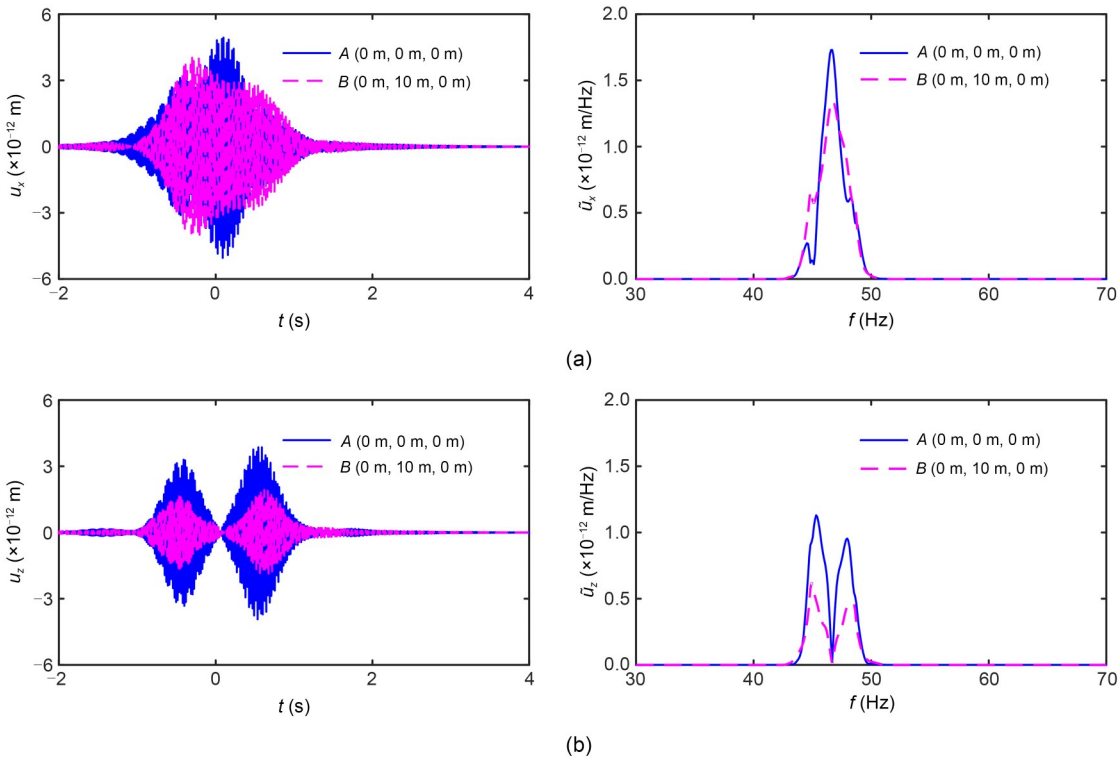

Fig. 7 Vertical displacement (a) and longitudinal displacement (b) in time (u_x and u_z) and frequency ($\tilde{u}_x$ and $\tilde{u}_z$) domain at A (0 m, 0 m, 0 m) and B (0 m, 10 m, 0 m) of the ground surface

a similar time history envelope at points A and B, and the displacement vibrations at point B were weaker than those at point A owing to damping effects. These phenomena can also be observed in the frequency domain results. Besides, it can be found from the results in the frequency domain that the response frequency spreads within a narrow frequency band around the critical frequency. The critical frequency band is determined by two effects (Xu and Ma, 2022): the moving effect, $f_{cr}=n_1 v/L+f_0$, and the Doppler effect, $f_{band}=f_{cr}/(1\pm v/c_R)$ (frequency band), where c_R is the Rayleigh wave velocity. The moving effect increased the critical frequency and the Doppler effect broadened the frequency band. The critical frequency f_{cr} was 46.7 Hz. Furthermore, at this critical frequency, the vertical vibration reached a maximum, whereas the longitudinal vibration reached a minimum.

For a clear inspection of the vibration attenuation characteristics of the ground surface, Fig. 8 illustrates the absolute instantaneous displacement response on the ground surface at time t=0 s under a spatially periodic harmonic load. The area concerned has dimensions of $y\in$[−40 m, 40 m] and $z\in$[−40 m, 40 m] in the y–z plane, and the load is immediately beneath (0 m, 0 m) at t=0 s. Overall, the exciting ground vibration is distributed mainly in the area $y\in$[−20 m, 20 m] and $z\in$[−20 m, 20 m] and decays undulatingly in the far field. Many troughs and peaks were observed in the entire field. A closer inspection of Fig. 8a shows that the wavelength behind the load is longer than that in front of the load, owing to the Doppler effect. In addition, the wavelength in the z-direction (the load moving direction) is longer than that in the y-direction, and concentric waves have imperfect circular distributions. This is because the waves generated in the tunnel structure travel much faster than those in the soil and contribute to the ground vibration. At this time instant, the maximum response appeared at a certain distance from (0 m, 0 m), and a vibration shadow emerged above the tunnel. The vertical vibration was distributed mainly in the area within a certain lateral distance from (0 m, 0 m), whereas the longitudinal vibration was distributed mainly in the area within a certain longitudinal distance from (0 m, 0 m). Notably, the absolute longitudinal displacement was approximately zero along z= 0 m, as the propagating waves at z=0 m were perpendicular to the axis y=0 m at the time instant t=0 s.

4.2 Parametric analysis

A wide range of factors that affect the vibration response characteristics on the ground were systematically investigated, including the load type, wavenumber in one periodicity length n_l, load frequency f_0, load velocity v, tunnel thickness h, buried depth of tunnel axis d, and number of soil layers n_s. The significance of our results to engineering applications is highlighted.

First, the effects of load type on the vibration responses were studied. Fig. 9 shows the vertical velocity responses at A (0 m, 0 m, 0 m) on the ground under a moving constant load (n_l=0, f_0=0 Hz), moving harmonic load (n_l=0, f_0=5 Hz), and moving spatially periodic harmonic load (n_l=1, f_0=5 Hz) in both the time and frequency domains. The responses under a constant load showed quasi-static behaviour, where the response frequency spread within the frequency range of f<2 Hz. Among the three types of loads, the moving harmonic

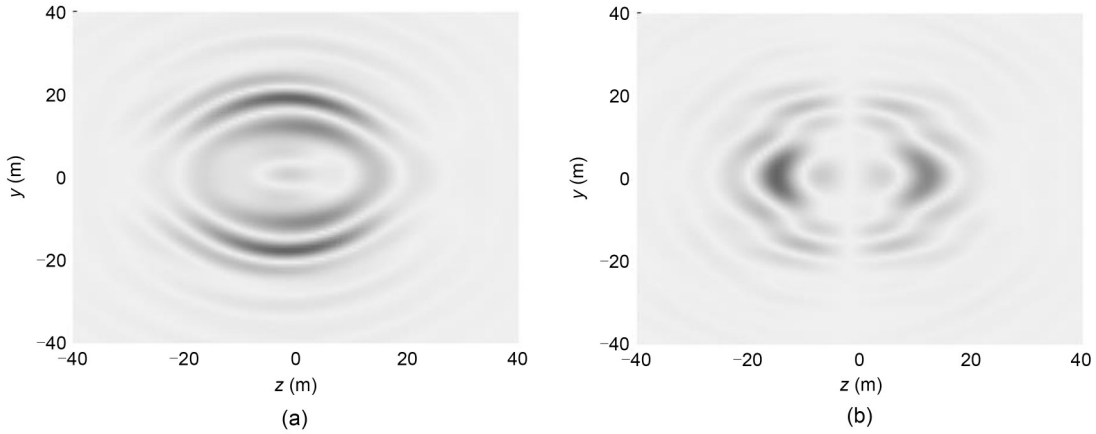

Fig. 8 Absolute instantaneous vertical displacement u_x (a) and longitudinal displacement u_z (b) on the ground surface at the time instant t=0 s

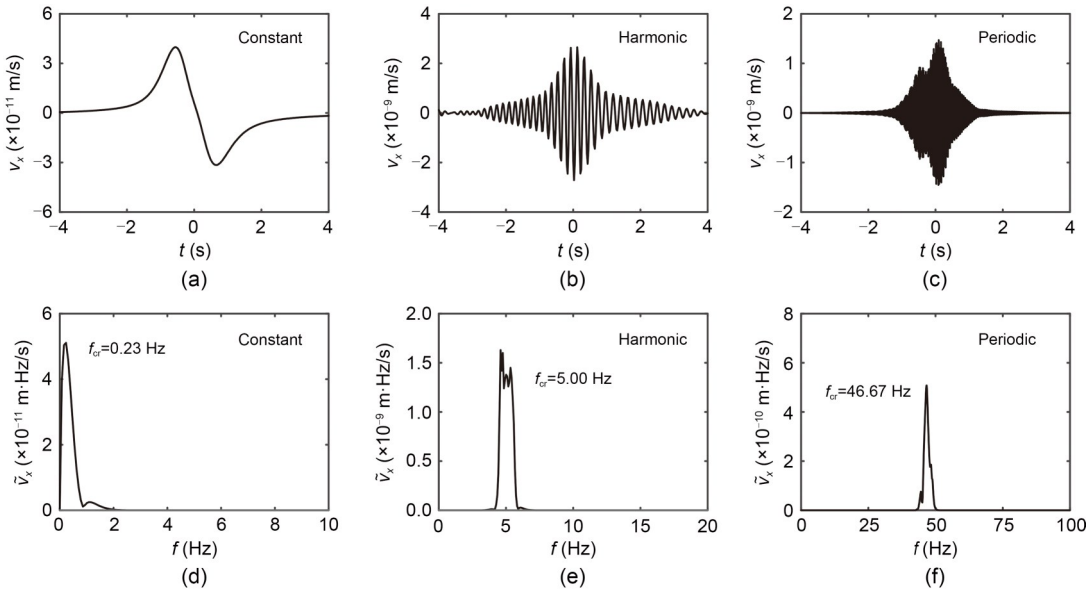

Fig. 9 Vertical velocities at *A* (0 m, 0 m, 0 m) on the ground surface under moving constant (a and d), harmonic (b and e), and spatially periodic harmonic (c and f) load in both time (a–c) and frequency (d–f) domains

load led to the strongest response on the ground surface. A denser time history was observed as the load type changed. The critical frequencies for the three cases were 0.23, 5.00, and 46.67 Hz, respectively. The Doppler effect was observed in all three cases, whereas the moving effect was found only in the case of the periodic harmonic load because it is caused by the spatial periodicity of the moving load. Also, the frequency band within which the response frequency mainly spread was wider in the case of the periodic harmonic load.

The effects of the wavenumber in one periodicity length n_l on the vertical displacement frequency spectrum and maximum vertical displacement along the y-axis on the ground are plotted in Fig. 10. Note that the vertical coordinates are logarithmic to allow better visualisation. In the frequency domain, as the wavenumber in one periodicity length n_l increased, the critical frequency increased consistently and the frequency band spread wider. Generally, a higher wavenumber results in a weaker displacement response on the ground surface. This is because more vibration energy in the higher frequency range is dissipated by soil. Except in the case n_l=0, the vertical displacements exhibited undulating behaviour along the y-axis, and vibration amplification effects were observed in some areas. This finding agrees with results from field measurements of vibration induced by metro train passaging that showed a ground vibration amplification area at a certain distance from the tunnel axis.

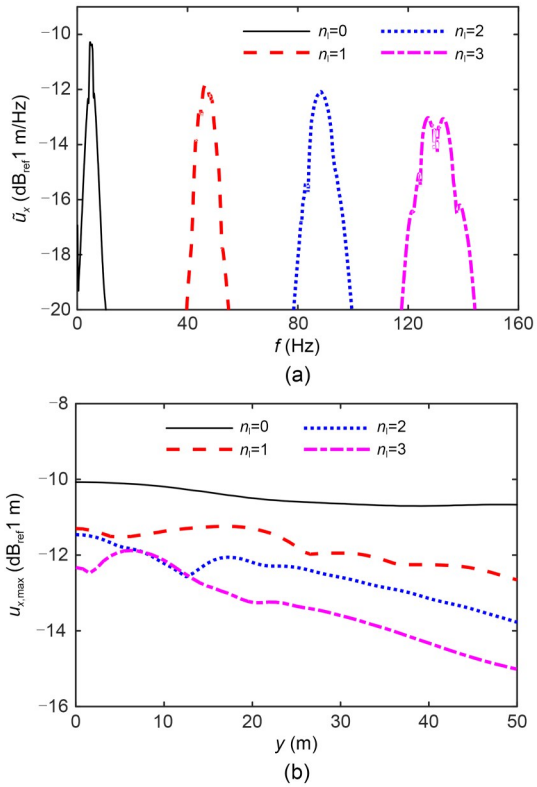

Fig. 10 Effects of the wavenumber in one periodicity length n_l on vertical displacement frequency spectrum at *A* (0 m, 0 m, 0 m) (a) and the maximum vertical displacement ($u_{x,\max}$) along the y-axis on the ground surface (b)

Fig. 11 shows the effects of the load frequency f_0 on the displacement frequency spectrum and the maximum

vertical displacement along the y-axis on the ground surface. As a general trend, an increase in the load frequency results in an increase in the displacement response critical frequency and frequency band owing to the moving and Doppler effects, but a decrease in the displacement response amplitude on the free surface. The displacement attenuation on the y-axis under the spatially periodic harmonic moving load exhibits undulating behaviour owing to the propagating waves in the free surface. The undulating behaviour becomes less obvious at higher load frequencies. The vibration amplification area seems to move toward the tunnel axis as f_0 increases. This may be caused by the shorter wavelengths of the ground propagating waves at higher frequencies. Fig. 12 is a plot of the amplitude of the displacement responses at A (0 m, 0 m, 0 m) and B (0 m, 10 m, 0 m) on the ground surface, owing to the spatially periodic harmonic load at various frequencies. Generally, under a spatially periodic harmonic moving load, the ground points vibrate more violently in the vertical direction than in the longitudinal direction. This is because the loads applied at the inverted arch of the tunnel are in the vertical direction. Typically, an increase in f_0 results in a decrease in the displacement response in both the vertical and longitudinal directions. However, the vibration attenuation shows a fluctuating behaviour with increasing load frequency.

Fig. 13 presents the vertical displacement frequency spectrum at A (0 m, 0 m, 0 m) and the instantaneous vertical displacement at time instant t=0 s along the y-axis on the ground surface under various load velocities. Similarly, owing to the moving and Doppler effects, a higher load velocity results in a higher critical frequency and a wider frequency band. Generally, the amplitudes of the displacement responses decrease with an increase in the load velocity (Figs. 13a and 13b). As shown in Fig. 13b, the wavelengths of the propagating waves on the ground surface are shortened by increasing load velocities. This is because the critical frequencies of the propagating waves are raised by

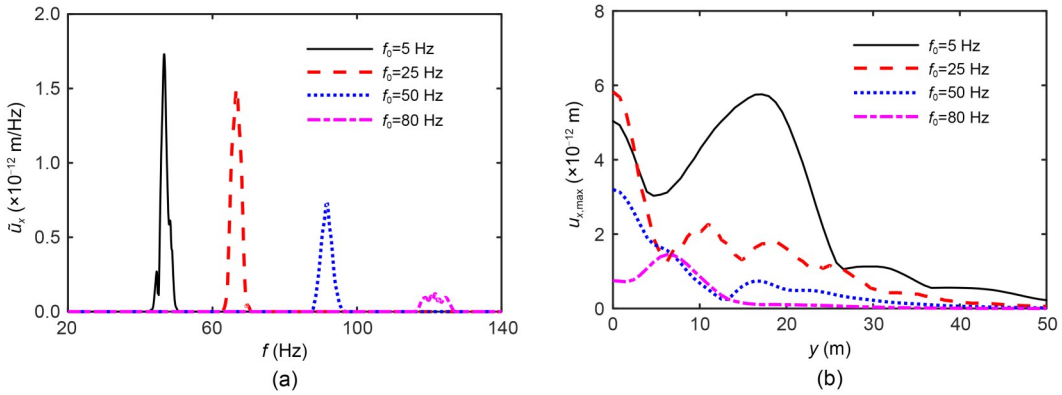

Fig. 11 Effects of load frequency f_0 on vertical displacement frequency spectrum at A (0 m, 0 m, 0 m) (a) and the maximum vertical displacement along the y-axis on the ground surface (b)

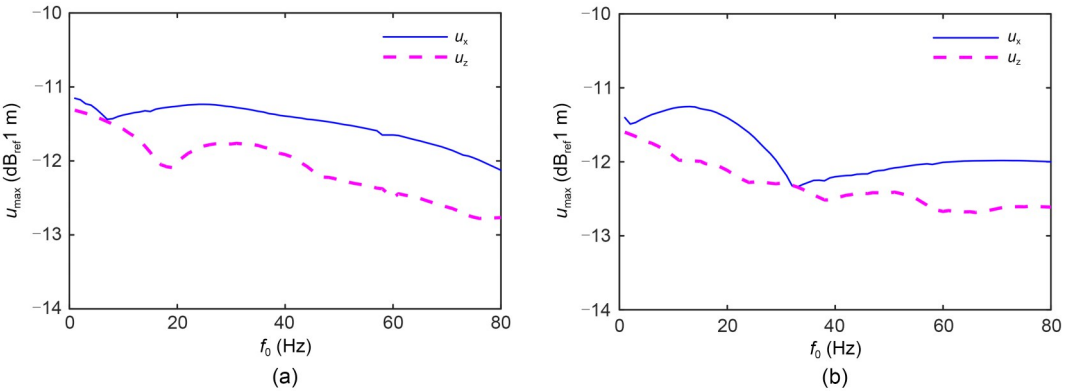

Fig. 12 Amplitudes of vertical and longitudinal displacements at A (0 m, 0 m, 0 m) (a) and B (0 m, 10 m, 0 m) (b) on the ground surface due to the spatially periodic harmonic load with various frequencies

the increase in load velocity, thus leading to shorter wavelengths.

Figs. 14 and 15 show the effect of the tunnel thickness and depth on the displacement frequency spectrum at A (0 m, 0 m, 0 m) and the instantaneous vertical displacement along the y-axis on the free surface. Variations in the tunnel thickness and depth have little impact on the critical frequency and frequency bands. As a general trend, an increase in tunnel depth reduces the level of vibration, because the soil dissipates more

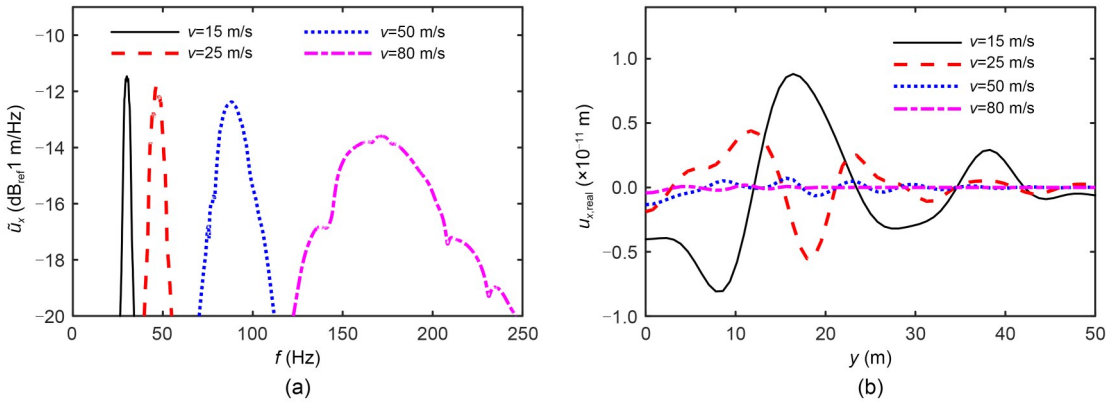

Fig. 13 Effects of load velocity on vertical displacement frequency spectrum $\tilde{u}_x$ at A (0 m, 0 m, 0 m) (a) and real part of instantaneous vertical displacement $u_{x,\mathrm{real}}$ at the time instant t=0 s along the y-axis on the ground surface (b)

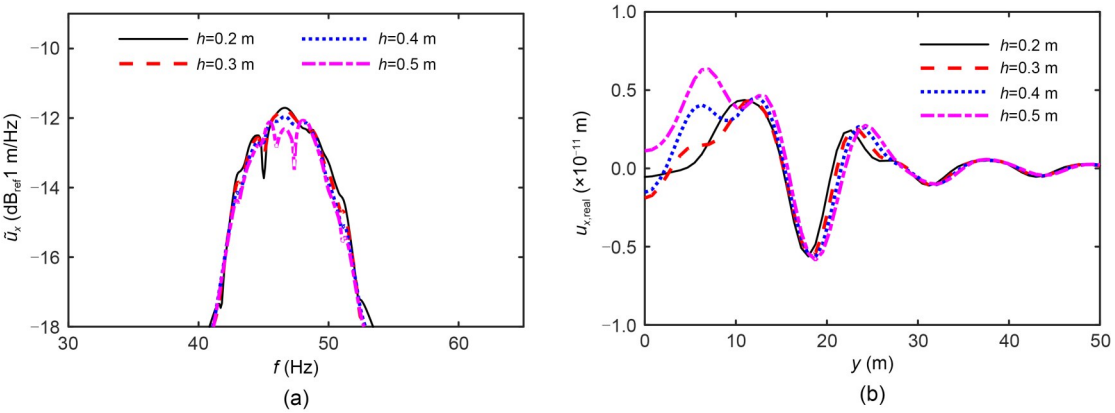

Fig. 14 Effects of tunnel thickness on vertical displacement frequency spectrum at A (0 m, 0 m, 0 m) (a) and real part of instantaneous vertical displacement along the y-axis on the free surface (b)

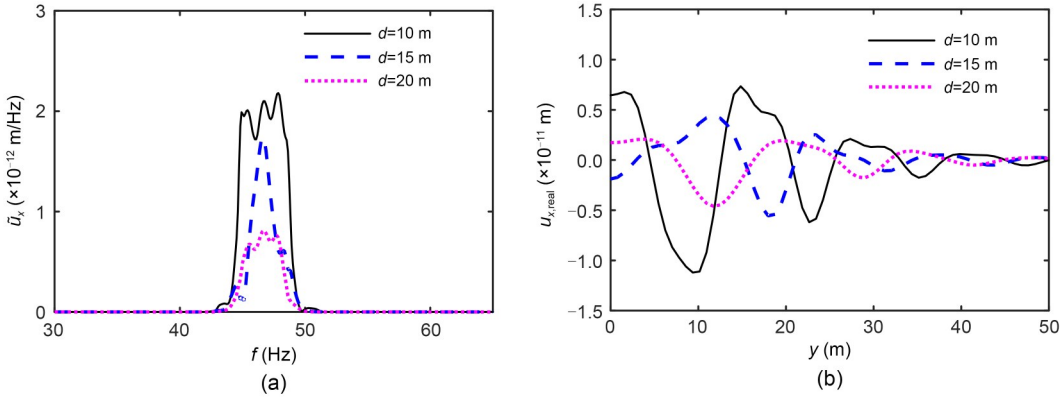

Fig. 15 Effects of tunnel depth on vertical displacement frequency spectrum at A (0 m, 0 m, 0 m) (a) and real part of instantaneous vertical displacement along the y-axis on the free surface (b)

of the energy of the propagating waves emanating from the deeper vibration source. Fig. 14b shows that a phase lag is caused by the variation in tunnel thickness, but this effect becomes insignificant in the far field. In the near field, the vibration level is amplified by the tunnel thickness. In practical applications, increasing the tunnel depth is an efficient measure to reduce the ground-borne vibration induced by underground vibration sources, whereas thickening the tunnel lining does little to attenuate the level of ground vibration.

Finally, the effect of the number of soil layers was investigated. Fig. 16 illustrates the effects of the number of soil layers on the ground-borne vibration under a spatially periodic harmonic moving load. In the case n_s, the material and geometric parameters of the first n_s soil layers were adopted, where the last soil layer extended to infinity. Variation in the number of soil layers had no effect on the critical frequency and frequency band. Generally, the ground-borne vibration level under n_s=1 was the highest. However, the vibration levels under n_s=2 and 3 were almost the same,

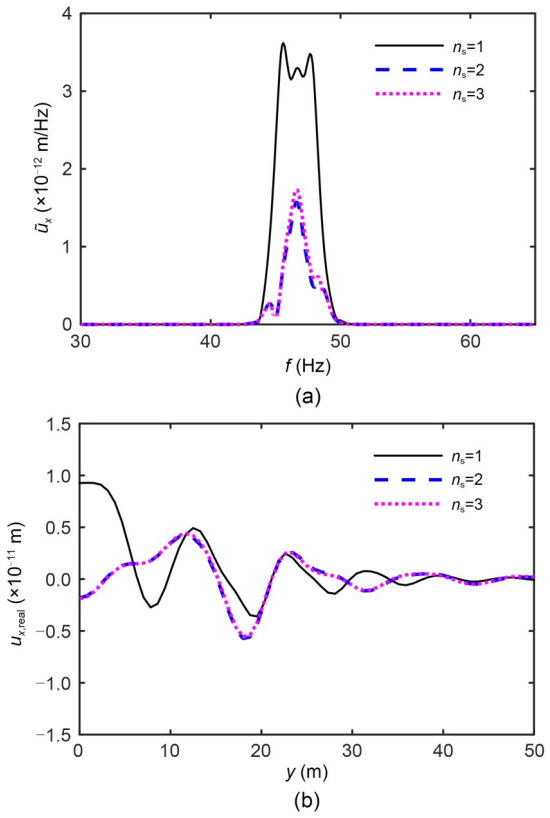

Fig. 16 Effects of the number of soil layers on vertical displacement frequency spectrum at A (0 m, 0 m, 0 m) (a) and real part of instantaneous vertical displacement along the y-axis on the free surface (b)

implying that the characteristics of the soil layer under the tunnel had little impact on the ground response. The wavelengths under n_s=2 and 3 were longer than those under n_s=1 because the propagating waves travelled faster in soil layer 2 under n_s=2 and 3, as listed in Table 2. This played an important role in the ground vibration characteristics. Variation in soil properties also led to the amplification of the vibration levels at y=20 m. In engineering applications, increasing the stiffness of the soil layers containing and beneath the tunnel may amplify the ground-borne vibration levels in some areas.

4.3 Discussion

A coupled periodic tunnel–soil analytical model was proposed to calculate the ground vibration response under a spatially periodic harmonic moving load. Based on this model, the general characteristics of the responses were investigated. Further, a parametric analysis was conducted to study the effects of a wide range of factors on responses. The moving effects and Doppler effects were observed.

Due to the generalised modal function applied in the derivation, this model is applicable only to the case under a moving point load. However, this periodic analytical model can be extended to cover the case of a fixed-point load using the generalised wavenumber technique. Then, the frequency response functions (FRFs) can be calculated and compared with those from the impact experiment.

For the assessment of metro train-induced environmental vibration, the track slab and moving train load should be further considered in the presented periodic analytical model. Then, the ground borne vibrations from underground trains can be obtained and compared with field measurements. As the analytical model requires little computer memory and computational time, it has the potential to assess the vibration levels of many sensitive sites along the metro line, which can provide vital information for vibration mitigation measures. This work will be conducted in future studies.

5 Conclusions

In this study, a novel coupled periodic tunnel–soil analytical model was proposed for predicting the ground-borne vibrations generated from a tunnel embedded in a multilayered half-space. General solutions

for all parts were derived, which were regarded as periodic in the longitudinal direction. The multilayered soils overlying the semi-infinite half-space were modeled using the transfer matrix method. The interactions between the tunnel and multilayered half-space were modeled by considering the transformation properties between the cylindrical and plane waves. The proposed model was validated by comparing the results under a moving constant and harmonic load with those from the literature. The characteristics of ground-borne vibrations under spatially periodic harmonic moving loads, and the effects of a wide range of factors on vibration responses, were systematically investigated. The following conclusions were drawn from the results.

(1) The proposed coupled periodic tunnel–soil analytical model is highly accurate, computationally efficient, and can be used to predict the ground-borne vibrations induced by train operations within a tunnel.

(2) In the time history, the vertical response reaches a maximum, whereas the longitudinal response reaches a minimum at the time instant when the load is immediately beneath the observation point. Both moving and Doppler effects can be excited by a spatially periodic harmonic moving load.

(3) Owing to moving and Doppler effects, the load type, load frequency, load velocity, and wavenumber in one periodicity length alter the critical frequency and frequency bandwidth. Variations in tunnel depth, tunnel thickness, and soil layer number have little impact on these features but give rise to a change in vibration amplitude. Increasing the tunnel depth was found to be an efficient way to reduce the level of ground-borne vibration.

(4) Under a spatially periodic harmonic moving load, a vibration amplification area exists at a certain horizontal distance from the tunnel axis. This should be considered to avoid potential excessive train-induced vibration that disturbs residents.

The current periodic analytical model is applicable only for the case of a moving point load. Future work could extend this model to cover the case of a fixed-point load, and to consider the track slab and the moving train load to assess metro train-induced environmental vibration levels.

Acknowledgments

This work is supported by the Fundamental Research Funds for the Central Universities of China (No. 2021JBM031) and the National Natural Science Foundation of China (No. 51978043).

Author contributions

Lihui XU wrote the first draft of the manuscript. Meng MA revised and edited the final version.

Conflict of interest

Lihui XU and Meng MA declare that they have no conflict of interest.

References

Boström A, Kristensson G, Ström S, 1991. Transformation properties of plane, spherical and cylindrical scalar and vector wave functions. *In*: Varadan VV, Lakhtakia A, Varadan VK (Eds.), Acoustic, Electromagnetic and Elastic Wave Scattering, Field Representations and Introduction to Scattering. Elsevier, Amsterdam, the Netherlands, p.165-210.

Clouteau D, Arnst M, Al-Hussaini TM, et al., 2005. Freefield vibrations due to dynamic loading on a tunnel embedded in a stratified medium. *Journal of Sound and Vibration*, 283(1-2):173-199. https://doi.org/10.1016/j.jsv.2004.04.010

Degrande G, Clouteau D, Othman R, et al., 2006. A numerical model for ground-borne vibrations from underground railway traffic based on a periodic finite element–boundary element formulation. *Journal of Sound and Vibration*, 293(3-5):645-666. https://doi.org/10.1016/j.jsv.2005.12.023

Doyle JF, 1997. Wave Propagation in Structures: Spectral Analysis Using Fast Discrete Fourier Transforms, 2nd Edition. Springer, New York, USA. https://doi.org/10.1007/978-1-4612-1832-6

Forrest JA, Hunt HEM, 2006a. A three-dimensional tunnel model for calculation of train-induced ground vibration. *Journal of Sound and Vibration*, 294(4-5):678-705. https://doi.org/10.1016/j.jsv.2005.12.032

Forrest JA, Hunt HEM, 2006b. Ground vibration generated by trains in underground tunnels. *Journal of Sound and Vibration*, 294(4-5):706-736. https://doi.org/10.1016/j.jsv.2005.12.031

François S, Schevenels M, Galvín P, et al., 2010. A 2.5D coupled FE–BE methodology for the dynamic interaction between longitudinally invariant structures and a layered halfspace. *Computer Methods in Applied Mechanics and Engineering*, 199(23-24):1536-1548. https://doi.org/10.1016/j.cma.2010.01.001

Gao GY, He JF, Yang CB, et al., 2011. Ground vibration induced by trains moving on saturated ground using 2.5D FEM. *Chinese Journal of Geotechnical Engineering*, 33(2):234-241 (in Chinese).

He C, Zhou SH, Di HG, et al., 2018. Analytical method for calculation of ground vibration from a tunnel embedded in a multi-layered half-space. *Computers and Geotechnics*, 99:149-164. https://doi.org/10.1016/j.compgeo.2018.03.009

He C, Zhou SH, Guo PJ, et al., 2019. Theoretical modelling of the dynamic interaction between twin tunnels in a multi-layered half-space. *Journal of Sound and Vibration*, 456:

65-85.
https://doi.org/10.1016/j.jsv.2019.05.025

Hussein MFM, Hunt HEM, 2009. A numerical model for calculating vibration due to a harmonic moving load on a floating-slab track with discontinuous slabs in an underground railway tunnel. *Journal of Sound and Vibration*, 321(1-2):363-374.
https://doi.org/10.1016/j.jsv.2008.09.023

Hussein MFM, François S, Schevenels M, et al., 2014. The fictitious force method for efficient calculation of vibration from a tunnel embedded in a multi-layered half-space. *Journal of Sound and Vibration*, 333(25):6996-7018.
https://doi.org/10.1016/j.jsv.2014.07.020

Jin H, Tian QR, Li Z, et al., 2022. Ability of vibration control using rubberized concrete for tunnel invert-filling. *Construction and Building Materials*, 317:125932.
https://doi.org/10.1016/j.conbuildmat.2021.125932

Kouroussis G, Connolly DP, Verlinden O, 2014. Railway-induced ground vibrations–a review of vehicle effects. *International Journal of Rail Transportation*, 2(2):69-110.
https://doi.org/10.1080/23248378.2014.897791

Lin KC, Hung HH, Yang JP, et al., 2016. Seismic analysis of underground tunnels by the 2.5D finite/infinite element approach. *Soil Dynamics and Earthquake Engineering*, 85:31-43.
https://doi.org/10.1016/j.soildyn.2016.03.005

Liu WF, Wu ZZ, Li CY, et al., 2022. Prediction of groundborne vibration induced by a moving underground train based on excitation experiments. *Journal of Sound and Vibration*, 523:116728.
https://doi.org/10.1016/j.jsv.2021.116728

Lombaert G, Degrande G, François S, et al., 2015. Groundborne vibration due to railway traffic: a review of excitation mechanisms, prediction methods and mitigation measures. *In*: Nielsen JCO, Anderson D, Gautier PE, et al. (Eds.), Noise and Vibration Mitigation for Rail Transportation Systems. Springer, Heidelberg, Germany, p.253-287.
https://doi.org/10.1007/978-3-662-44832-8_33

Lopes P, Ruiz JF, Alves Costa P, et al., 2016. Vibrations inside buildings due to subway railway traffic. Experimental validation of a comprehensive prediction model. *Science of the Total Environment*, 568:1333-1343.
https://doi.org/10.1016/j.scitotenv.2015.11.016

Ma LX, Liu WN, 2018. A numerical train–floating slab track coupling model based on the periodic-Fourier-modal method. *Proceedings of the Institution of Mechanical Engineers, Part F: Journal of Rail and Rapid Transit*, 232(1):315-334.
https://doi.org/10.1177/0954409716668552

Ma LX, Liu WN, Jiang YJ, et al., 2017. Metro train-induced vibration influences on surrounding environments based on sliced finite element-infinite element coupled model. *Journal of Vibration and Shock*, 36(15):111-117 (in Chinese).
https://doi.org/10.13465/j.cnki.jvs.2017.15.017

Ma LX, Zhang C, Ouyang HJ, et al., 2021. 2.5D modelling of wave propagation in longitudinally curved viscoelastic structure using a coupled FEM-PML approach. *Engineering Structures*, 226:111337.
https://doi.org/10.1016/j.engstruct.2020.111337

Ma M, Liu WN, Qian CY, et al., 2016. Study of the train-induced vibration impact on a historic bell tower above two spatially overlapping metro lines. *Soil Dynamics and Earthquake Engineering*, 81:58-74.
https://doi.org/10.1016/j.soildyn.2015.11.007

Ma M, Liu WN, Liu WF, 2020. Research progresses of prediction method and uncertainty of train-induced environmental vibration. *Journal of Traffic and Transportation Engineering*, 20(3):1-16 (in Chinese).
https://doi.org/10.19818/j.cnki.1671-1637.2020.03.001

Ma M, Li MH, Qu XY, et al., 2022. Effect of passing metro trains on uncertainty of vibration source intensity: monitoring tests. *Measurement*, 193:110992.
https://doi.org/10.1016/j.measurement.2022.110992

Metrikine AV, Vrouwenvelder ACWM, 2000. Surface ground vibration due to a moving train in a tunnel: two-dimensional model. *Journal of Sound and Vibration*, 234(1):43-66.
https://doi.org/10.1006/jsvi.1999.2853

Pilant WL, 1979. Elastic Waves in the Earth. Elsevier, New York, USA.

Sheng X, Jones CJC, Thompson DJ, 2002. Moving Green's Functions for a Layered Circular Cylinder of Infinite Length. ISVR Technical Memorandum No. 885, University of Southampton, Southampton, UK.

Sheng X, Jones CJC, Thompson DJ, 2005. Modelling ground vibration from railways using wavenumber finite- and boundary-element methods. *Proceedings of the Royal Society A: Mathematical, Physical and Engineering Sciences*, 461(2059):2043-2070.
https://doi.org/10.1098/rspa.2005.1450

Xu LH, Ma M, 2020. Study of the characteristics of train-induced dynamic SIFs of tunnel lining cracks based on the modal superposition approach. *Engineering Fracture Mechanics*, 233:107069.
https://doi.org/10.1016/j.engfracmech.2020.107069

Xu LH, Ma M, 2022. Dynamic response of the multilayered half-space medium due to the spatially periodic harmonic moving load. *Soil Dynamics and Earthquake Engineering*, 157:107246.
https://doi.org/10.1016/j.soildyn.2022.107246

Xu LH, Ma M, Cao RN, et al., 2022. Effect of longitudinally varying characteristics of soil on metro train-induced ground vibrations based on wave propagation analysis. *Soil Dynamics and Earthquake Engineering*, 152:107020.
https://doi.org/10.1016/j.soildyn.2021.107020

Yang YB, Li J, 2022. 2.5D prediction of soil vibrations due to railway loads by the isogeometric analysis with scaled boundary. *Engineering Analysis with Boundary Elements*, 134:341-359.
https://doi.org/10.1016/j.enganabound.2021.10.012

Yang YB, Liang XJ, Hung HH, et al., 2017. Comparative study of 2D and 2.5D responses of long underground tunnels to moving train loads. *Soil Dynamics and Earthquake Engineering*, 97:86-100.
https://doi.org/10.1016/j.soildyn.2017.02.005

Yang YB, Liu SJ, Chen W, et al., 2021. Half-space response to trains moving along curved paths by 2.5D finite/infinite

element approach. *Soil Dynamics and Earthquake Engineering*, 145:106740. https://doi.org/10.1016/j.soildyn.2021.106740

Yuan ZH, Boström A, Cai YQ, 2017. Benchmark solution for vibrations from a moving point source in a tunnel embedded in a half-space. *Journal of Sound and Vibration*, 387: 177-193. https://doi.org/10.1016/j.jsv.2016.10.016

Yuan ZH, Cao ZG, Tang H, et al., 2021. Analytical layer element with a circular cavity and its application in predicting ground vibrations from surface and underground moving sources. *Computers and Geotechnics*, 137:104262. https://doi.org/10.1016/j.compgeo.2021.104262

Zhang ZH, Zhang XD, Tang Y, et al., 2018. Discrete element analysis of a cross-river tunnel under random vibration levels induced by trains operating during the flood season. *Journal of Zhejiang University-SCIENCE A (Applied Physics & Engineering)*, 19(5):346-366. https://doi.org/10.1631/jzus.A1700002

Zhou SH, He C, Guo PJ, et al., 2019. Dynamic response of a segmented tunnel in saturated soil using a 2.5D FE-BE methodology. *Soil Dynamics and Earthquake Engineering*, 120:386-397. https://doi.org/10.1016/j.soildyn.2019.02.017

Zou C, Moore JA, Sanayei M, et al., 2022. Impedance model of train-induced vibration transmission across a transfer structure into an over track building in a metro depot. *Journal of Structural Engineering*, 148(11):04022187. https://doi.org/10.1061/(ASCE)ST.1943-541X.0003482

Electronic supplementary materials

Sections S1–S3, Eqs. (S1)–(S47)